Afterslip on Conjugate Faults of the 2020 M_w 6.3 Nima Earthquake in the Central Tibetan Plateau: Evidence from InSAR Measurements

Shunying Hong[*1], Mian Liu[2], Xin Zhou[3], Guojie Meng[1], and Yanfang Dong[1]

ABSTRACT

Afterslip could help to reveal seismogenic fault structure. The 2020 M_w 6.3 Nima earthquake happened in a pull-apart basin within the Qiangtang block, central Tibetan plateau. Previous studies have explained the coseismic and early (< 6 mo) postseismic deformation by rupture and afterslip on a normal fault bounding the western side of the basin. Here, we resolved the 19-month Interferometric Synthetic Aperture Radar-measured sequences of postseismic displacements that revealed a second postseismic displacement center ~12 km to the east of the main fault. Fitting the postseismic displacement requires afterslip on both the main fault and an antithetic fault that probably forms a y-shaped pair of conjugate faults in a negative flower structure. Stress-driven afterslip models suggest that the required afterslip on the antithetic fault could be triggered by coseismic rupture of the main fault or by a simultaneous rupture on the antithetic fault. The afterslip on both faults occurred mainly up-dip to the coseismic slip and has released moment ~15%–19% of that by the coseismic rupture. These results provide insights into active extension in the central Tibetan plateau and highlight the complex nature of fault rupture and afterslip.

KEY POINTS

- Postseismic Interferometric Synthetic Aperture Radar measurements indicate afterslip on a pair of y-shaped faults.
- Coseismic rupture on the secondary fault cannot be resolved but is likely.
- Afterslip on the secondary fault could be triggered by coseismic rupture of the main fault.

Supplemental Material

INTRODUCTION

Intracontinental earthquakes often involve spatially complex fault ruptures (e.g., Simons et al., 2002; Nissen et al., 2016). In addition to triggered aftershocks on both host faults and their neighboring faults by stress perturbation (e.g., Freed, 2005; Van der Elst and Brodsky, 2010), geodetic measurements have revealed complex afterslip on multiple ruptured fault planes (e.g., Maurer et al., 2022). Afterslip has been recognized as an important part of the cycles of strain energy accumulation and release in fault systems (e.g., Avouac, 2015). It can release a significant portion of seismic moment (e.g., Hong and Liu, 2021), provide clues to changes of fault friction (e.g., Wang and Bürgmann, 2020), and delineate fault structures (e.g., Barnhart et al., 2018). Here, we investigate complex afterslip of the 2020 M_w 6.3 Nima earthquake using Interferometric Synthetic Aperture Radar (InSAR) data.

On 22 July 2020, an M_w 6.3 earthquake struck Nima, China, in the Qiangtang block of the central Tibetan plateau. The seismic fault is a western branch of the Yibu Chaka normal fault (Ji et al., 2021; Li, Li, Tapponnier, et al., 2021; Li, Li, Tan, and Lu, 2021; Qiu et al., 2021), which bounds a small pull-apart basin, the Yibu Chaka basin, in a releasing stepover of the sinistral Riganpei Co-Yibu Chaka-Jiangai Zangbo fault (RYJF) zone (Li, Li, Tapponnier, et al., 2021; Fig. 1). Recent normal-faulting earthquakes here, including the 2012 M_w 4.9 and 2019 M_w 5.0 earthquakes (Fig. 1), indicate active extension (Li, Li, Tapponnier, et al., 2021) and provide insights of present-day crustal kinematics in the central Tibetan plateau (e.g., Taylor et al., 2003).

The InSAR data acquired within six months after the earthquake have been used to constrain postseismic deformation

1. Institute of Earthquake Forecasting, China Earthquake Administration, Beijing, China, https://orcid.org/0000-0002-6259-1323 (SH); https://orcid.org/0000-0002-6584-0380 (GM); https://orcid.org/0000-0001-7490-924X (YD);
2. Department of Geological Sciences, University of Missouri, Columbia, Missouri, U.S.A.; 3. National Institute of Natural Hazards, Beijing, China

*Corresponding author: hongsy@ief.ac.cn

Cite this article as Hong, S., M. Liu, X. Zhou, G. Meng, and Y. Dong (2023). Afterslip on Conjugate Faults of the 2020 M_w 6.3 Nima Earthquake in the Central Tibetan Plateau: Evidence from InSAR Measurements, Bull. Seismol. Soc. Am. XX, 1–15, doi: 10.1785/0120220247

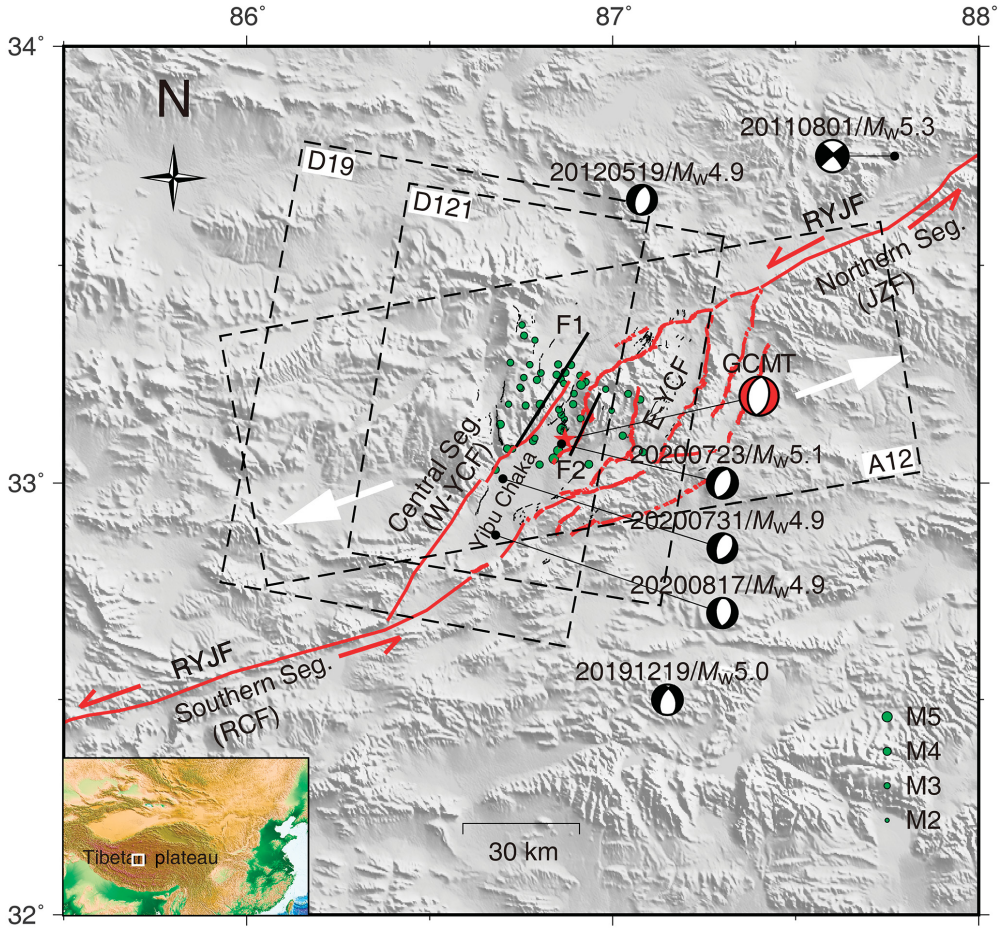

Figure 1. Tectonic map of the epicentral region of the 2020 Nima earthquake, which occurred within a stepover pull-apart basin in the central segment of the Riganpei Co-Yibu Chaka-Jiangai Zangbo fault (RYJF, red lines). F1 is the main seismic fault for the earthquake; F2 is a secondary fault inferred from postseismic deformation. The focal mechanism solutions for the mainshock (red) and main aftershocks and historical earthquakes (black), from the Global Centroid Moment Tensor (Global CMT). The green dots are aftershocks three months after the mainshock, from the China Earthquake Data Center (CEDC). The dashed boxes show the postseismic Interferometric Synthetic Aperture Radar (InSAR) data coverage of A12, D121, and D19 tracks (Table S2). The fault traces are from Li, Li, Tapponnier et al. (2021). E-YCF, east branch of Yibu Chaka fault; JZF, Jiangai Zangbo fault; RCF, Riganpei Co fault; Seg., segment; W-YCF, west branch of Yibu Chaka fault. Lower-left inset shows the location of the main map.

and afterslip (Yang et al., 2021; Gao et al., 2022). Yang et al. (2021) suggested that afterslip on a branch fault ~2 km west of the surface projection of the seismic fault is likely responsible for the ~6 mo postseismic displacement measured by the ascending orbit (track 12). They suggested that the seismic fault possibly has a listric subsurface structure. Gao et al. (2022) used a curved fault model ~2–3 km west of the coseismic rupture to explain the ~4 mo postseismic displacement of ascending orbit (track 12) and descending orbit (track 121). However, their single-fault model does not explain the second displacement center east to the host fault in their postseismic deformation field (Gao et al., 2022). This second displacement center in track 121 possibly indicates complex fault slip but was not well resolved in the previous studies (Yang et al., 2021; Gao et al., 2022).

In this study, we used the ~19 month postseismic Sentinel-1A/1B data from three line of sight (LoS) directions of ascending orbit (track 12) and descending orbit (tracks 121 and 19) to resolve postseismic deformation and afterslip. Our results confirm the second center of postseismic displacement ~12 km to the east of the main fault, also shown in the results of Gao et al. (2022). We suggest that the postseismic displacement field results from afterslip on both the main fault and a secondary fault, likely an antithetic fault, that forms a pair of y-shaped conjugate faults in a negative flower structure. Either triggered by rupture of the main fault or by simultaneous rupture on the antithetic fault, afterslip of the Nima earthquake provides useful insight into complex rupture and postseismic deformation as well as active extension in central Tibet.

COSEISMIC AND POSTSEISMIC DEFORMATION

InSAR data and processing

We processed Sentinel-1 single look complex (SLC) data (Tables S1, S2, available in the supplemental material to this article) from the ascending orbit (track 12) and the descending orbit (tracks 121 and 19), referred to as A12, D121, and D19 in this study. We adopted a "two-pass D-InSAR processing" approach (e.g., Massonnet et al., 1993) to process the coseismic data (Table S1) and extracted the coseismic deformation fields (Fig. 2a–c), with support of the InSAR Scientific Computing Environment (ISCE; Rosen et al., 2012). The topographic data from the Shuttle Radar Topography Mission with a spatial resolution of ~30 m was used to simulate and remove the topographic phases. The interferograms were unwrapped by the Statistical-cost, Network-flow Algorithm for Phase Unwrapping method (Chen and Zebker, 2002) and were subsequently transferred into displacements. We compared our coseismic deformation field (Fig. 2a–c) with that corrected

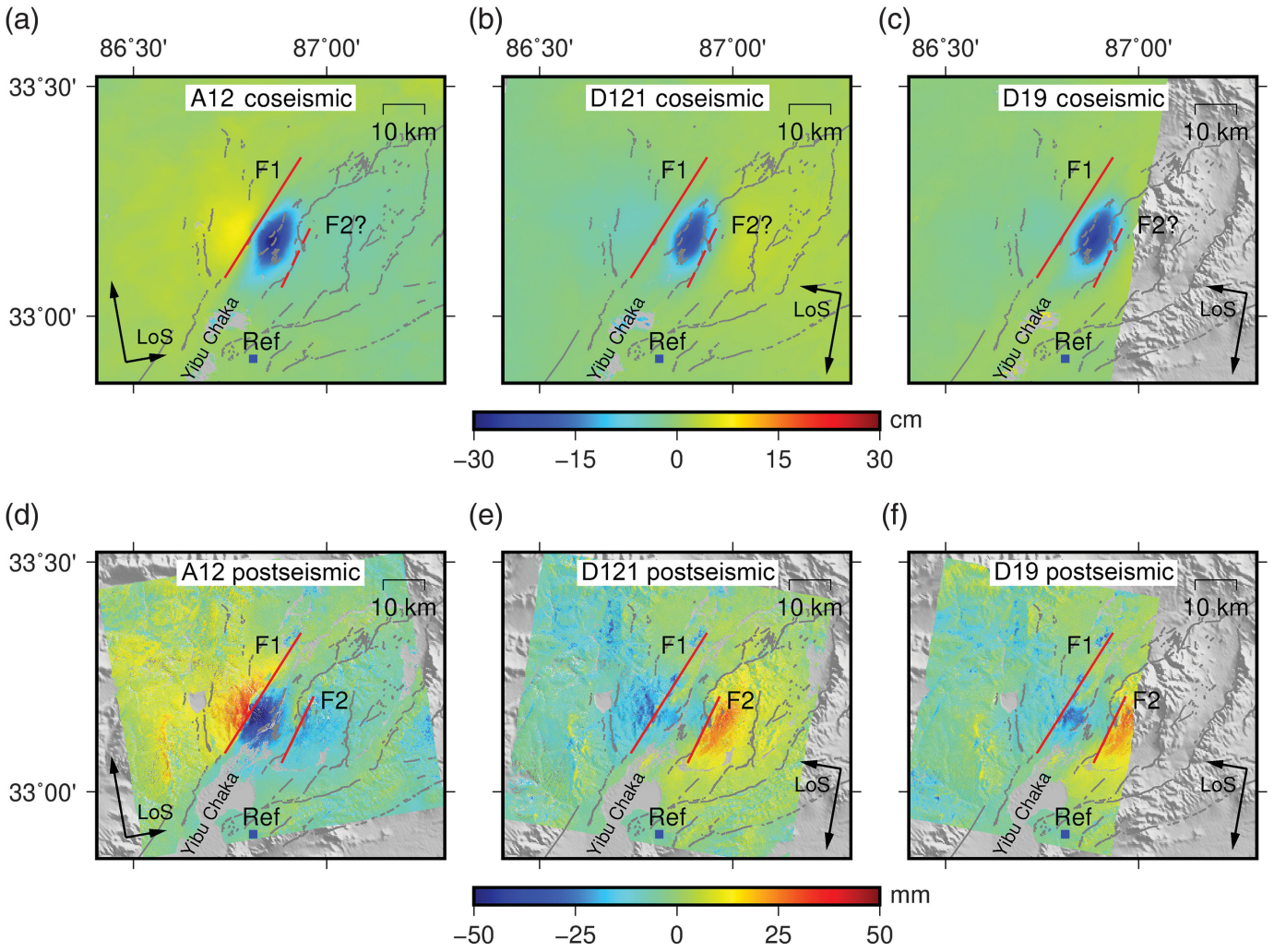

Figure 2. InSAR deformation fields. (a–c) Coseismic displacements of (a) the ascending orbit A12 and (b,c) the descending orbits D121 and D19, respectively. Positive values represent movement in line of sight (LoS) direction toward the Synthetic Aperture Radar (SAR) satellite platform; negative values indicate motion in the opposite direction. (d–f) Accumulated postseismic displacements (over ⍰19 months) of (d) the A12, (e) the D121, and (f) the D19 tracks, resolved by the fitting method (Text S1). Blue square is the reference location of InSAR measurement. F1 and F2 are the two faults shown in Figure 1. Ref, reference.

for topography-correlated atmospheric delays by Yang et al. (2021); the discrepancy is few and negligible (Fig. S1). The sparse vegetation coverage and relatively flat topography in this epicentral area helped to maintain interference coherence. The short temporal interval (12 days) and perpendicular baselines (<110 m; Table S1) of the coseismic interferograms also help to maintain the coherence and reduce the effect of atmospheric delay and topography error. Thus, the atmospheric error is negligible compared with the strong coseismic signal.

For postseismic deformation, the SLC data (Table S2) were first coregistered in the ISCE. There are altogether 49 acquisitions for the A12 track from 30 July 2020 to 10 March 2022, 50 acquisitions for the D121 from 26 July 2020 to 6 March 2022, and 36 acquisitions for the D19 from 25 July 2022 to 23 December 2021. The reference image for the A12, D121, and D19 tracks is acquired on 8 April, 4 April, and 3 April 2021, respectively. Then, the displacement time series were resolved by the single-reference Persistent Scatterer InSAR (PS-InSAR) method implemented in the Standford Method for Persistent Scatterers (StaMPS v.4.1b; Hooper et al., 2007, 2012), based on the previously coregistered SLC. The StaMPS technique allows for detecting nonlinear displacement signals without prior assumption of the deformation model (Hooper et al., 2007). The initial persistent scatterers points were weeded and merged into a grid size of 120 m with a standard derivation threshold of 1.5. The merged phases were then unwrapped by the "3D" method (Hooper and Zebker, 2007), and filtered out of the spatially correlated look angle error and the atmosphere and orbit errors of the reference SLC. The atmospheric noises on the secondary SLCs were estimated and removed by a time-then-space filtering method (Ferretti et al., 2001). A high-pass filtering in time with a window of 30 days (by try-and-error), then a low-pass filtering in space with a wavelength of 100 m, was used to estimate these atmospheric noises.

Text S1 provides the details of InSAR data processing for deriving coseismic and postseismic deformation fields.

Seasonal signals should be removed from the displacement sequences for a reasonable estimation of postseismic accumulated displacements and time series. We used the fitting method (Hong and Liu, 2021) to distinguish and remove seasonal signals from the time series (e.g., for the D121 track in Fig. S2) of the PS-InSAR measurement (Text S1). After removing the seasonal signals, the postseismic displacement sequences (e.g., for the D121 track in Fig. S3) and the accumulated postseismic displacements (Fig. 2d–f) were resolved. One point in the D121 track (Figs. S2, S3) was selected to illustrate our fitting method (Fig. S4). One small region (1 km × 1 km) in the D121 track (Figs. S2, S3) was also selected to show the time series at various pixels with and without the correction of seasonal signals (Fig. S5). For the afterslip inversion, we also interpolated the postseismic displacement sequences of the D121 and D19 tracks with the same acquisition periods as the A12 track (Table S2). The same reference location was defined for the coseismic and postseismic deformation fields, and both were downsampled with the quadtree method for the simulation analysis.

Coseismic deformation

Coseismic deformation fields extracted from ascending orbit (Fig. 2a) and descending orbit data (Fig. 2b,c) are similar to previous studies (Li, Li, Tan, and Lu, 2021; Li, Li, Tapponnier, et al., 2021). Table S1 provides the acquisition time of the three coseismic interference pairs. The first-order characteristics of the coseismic deformation fields include one range-increasing center along the LoS direction in the three-viewing geometry, indicating dominant normal faulting of the 2020 Nima earthquake. The maximum LoS subsidence is about 30 cm for the A12, 24 cm for D121, and 26 cm for D19 tracks.

Postseismic deformation

The accumulated postseismic displacements over ⍰19 months derived from the different viewing geometry of ascending and descending orbits are illustrated in Figure 2d–f. The accumulated displacement in LoS direction is −70 to 48 mm for A12, −44 to 40 mm for D121, and −41 to 39 mm for D19 tracks. The postseismic displacement time series after removing seasonal signals for the D121 track is illustrated in Figure S3 as an example. This postseismic displacement sequence is more reasonable, compared with that without filtering seasonal signals (Fig. S2).

The postseismic deformation fields (Fig. 2d–f) show clearly different characteristics from those of the coseismic deformation (Fig. 2a–c). Specifically, the postseismic deformation fields reveal two displacement centers. One center is near the main host fault (named F1 in this study), also identified in previous studies (Li, Li, Tapponnier, et al., 2021; Yang et al., 2021; Gao et al., 2022). The second displacement center is ⍰12 km east of F1 (Fig. 2e,f), indicating possible postseismic slip on another fault (named F2 in this study). This second displacement center was also seen in the results of Gao et al. (2022) with ⍰4 mo of postseismic measurement, but it was not well resolved or fitted by their single-fault model.

COSEISMIC SLIP

Fault geometry model

First, we used the coseismic displacement (Fig. 2a–c) to constrain the seismic host fault (F1). We determined its geometry by the coseismic deformation fields, using the Bayesian earthquake analysis tool (Vasyura-Bathke et al., 2020; Text S2, Fig. S6). The earth structure used here is a layered elastic half-space of CRUST 2.0 (Bassin et al., 2000). The optimal solution of the fault geometry parameters of F1 (dip = 49°) is shown in Figure S6 and Table S3. The result is similar to that resolved by the previous studies (Li, Li, Tan, and Lu, 2021; Li, Li, Tapponnier, et al., 2021; Yang et al., 2021; Gao et al., 2022). An enlarged fault model of F1 (length = 34 km, width = 20 km) based on these geometry parameters (Table S3) was adopted to model the distribution of coseismic slip and afterslip. We found that the surface projection of F1 inverted by the coseismic deformation fields was generally consistent with the postseismic displacement boundary in the A12 track (Fig. 2d).

We then determined the fault trace location of the secondary fault (F2) by the positive and negative displacement boundary of the second postseismic deformation center in the D121 and D19 tracks (Fig. 2e,f). The location of F2 is generally consistent with previously identified faults (Li, Li, Tapponnier, et al., 2021; Gao et al., 2022) on the eastern side of the Yibu Chaka basin (Fig. S7). The dip of F2 is determined to be 55°, by minimizing the root mean square residuals between the predicted and observed postseismic displacements (Fig. S8, Text S3). F2 dips to F1 and is likely an antithetic fault of F1, based on the geological field investigation of the fault system here (Gao et al., 2022). We set the width of F2 to be 10 km, which would make F2 to reach F1 and form a y-shaped negative flower fault structure (e.g., Harding, 1985; Gao et al., 2022).

Coseismic-slip model

The secondary fault F2 is indicated by the postseismic deformation fields (Fig. 2d–f). It is not clear whether it ruptured together with F1. Here, we first test the possibility of F2 rupture by inverting and comparing the coseismic-slip model in two cases: coseismic slip only on F1 (case-I) or coseismic slip on both F1 and F2 (case-II), respectively; the latter case was not considered in previous studies (Li, Li, Tan, and Lu, 2021; Li, Li, Tapponnier, et al., 2021; Yang et al., 2021; Gao et al., 2022). The Steepest Decent Method (SDM, Wang et al., 2013) was used to invert for coseismic slip. The fault planes of F1 and F2 were discretized into 2 km × 2 km patches. The smooth factor of 0.03 was selected by the trade-off between misfit

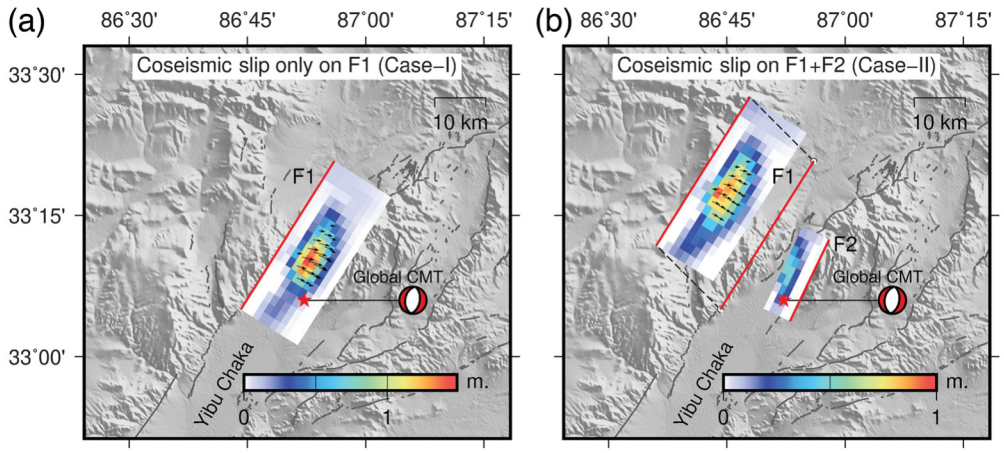

Figure 3. Inverted coseismic-slip model based on (a) the single-fault (F1) rupture model (case-I) and (b) the double-fault (F1 + F2) rupture model (case-II). Black arrows represent the rake angle and magnitude of coseismic fault slip.

and roughness for the coseismic slip. Equal weight was adopted for the downsampled deformation fields of the A12, D121, and D19 tracks.

The results for case-I are illustrated in Figure 3a. The maximum slip is ⍰1.5 m at a depth of ⍰7.0 km. Most fault slip was distributed over a length of ⍰16 km, in a depth range of 5–10 km. The average rake is about −73°, indicating a dominantly normal fault rupture. The seismic moment released by this model is $4{:}32 \times 10^{18}$ N · m (taking the shear modulus to be 30 GPa), equivalent to a magnitude M_w 6.36 earthquake. The coseismic slip of this single-fault model is similar to that of previous studies (e.g., Li, Li, Tapponnier, et al., 2021).

The results of case-II (i.e., rupture of F1 and F2) are shown in Figure 3b. Coseismic slip on F2 was not considered in previous studies (e.g., Li, Li, Tapponnier, et al., 2021) but is possible. The geometry of F1 and F2 (Table S3) suggests that they may be a pair of y-shaped conjugate faults in a negative flower structure. We found that most coseismic slip occurred on F1; the slip distribution is similar to that of the single-fault rupture model but with a smaller amplitude (Fig. 3b vs. Fig. 3a). The slip on F2 occurred only in the deep part where F2 probably connects with F1. The released seismic moment on F1 is $⍰3{:}67 \times 10^{18}$ N · m, and on F2 is $⍰0{:}66 \times 10^{18}$ N · m. The total moment release is $⍰4{:}33 \times 10^{18}$ N · m, nearly identical to that of the single-fault model. This double-fault rupture model explains the coseismic deformation fields equally well as the single-fault rupture model (Fig. 4), as evidenced also from the residual distribution (Fig. S9).

AFTERSLIP

In this section, we constrain afterslip based on the single-fault (F1) and double-fault (F1 + F2) models, using both a kinematic inversion method and a stress-driven forward method.

Inverted afterslip

The afterslip was inverted using the constraints of the accumulated postseismic deformation fields (Fig. 2d–f), following the SDM procedure (Wang et al., 2013). To distinguish the inverted afterslip from that of stress-driven model, we call it "kinematic afterslip" or KA in this study. Same as in our coseismic-slip inversion, a layered crustal structure of Crust 2.0, a smooth factor of 0.03, and an equal weight of different InSAR data were adopted. Both the single-fault (F1) and double-fault (F1 + F2) models were tested, with a discretized patch size of 2 km × 2 km. The corresponding displacement residuals were compared for the preferred fault model.

The KA inverted by the single-fault and double-fault models is shown in Figure 5a and Figure 5b, respectively. For the single-fault KA model, some afterslip overlaps with the coseismic-slip center, similar to earlier studies (Yang et al., 2021; Gao et al., 2022) but with a larger amplitude (due to a longer observation period). In the double-fault KA model, most afterslip on F1 occurred in the upper dip of the coseismic-slip area, shallower than that of the single-fault model (Fig. 5a) and that in previous studies (Yang et al., 2021; Gao et al., 2022). The maximum afterslip on F1 is ⍰18 cm, occurred at a depth of ⍰2.5 km with a rake angle of −48°. The afterslip on F2 has a maximum value of ⍰9 cm at a depth of ⍰5.7 km. The mean rake angle is −37° for F1 and −62° for F2, indicating more left-lateral slip component in the afterslip (Fig. 5b) than in the coseismic slip (Fig. 3).

The double-fault KA model fits the postseismic deformation fields better than the single-fault KA model, especially near F2 in the D121 and D19 tracks (Fig. 6). The residuals of the postseismic displacements predicted by the afterslip on F1 alone are distinctly greater than those by the double-fault (F1 + F2; Fig. S10). Thus, the double-fault KA model is preferred.

To avoid the influence of the fault patches without substantial afterslip, we selected a 24 km × 12 km area (dashed rectangle in Fig. 5b) of F1 where most afterslip occurred, to calculate the released seismic moment by F1. For F2, we used the whole fault plane to calculate the released seismic moment. Within the ⍰19 months after the mainshock, the released seismic moment is $⍰4{:}72 \times 10^{17}$ N · m on F1 and $⍰1{:}96 \times 10^{17}$ N · m on F2, respectively. The total released seismic moment is $⍰6{:}68 \times 10^{17}$ N · m, equivalent to a magnitude M_w 5.82 earthquake. This moment released by afterslip is approximately 15.4% of that by the coseismic slip, larger than that (⍰8%) from

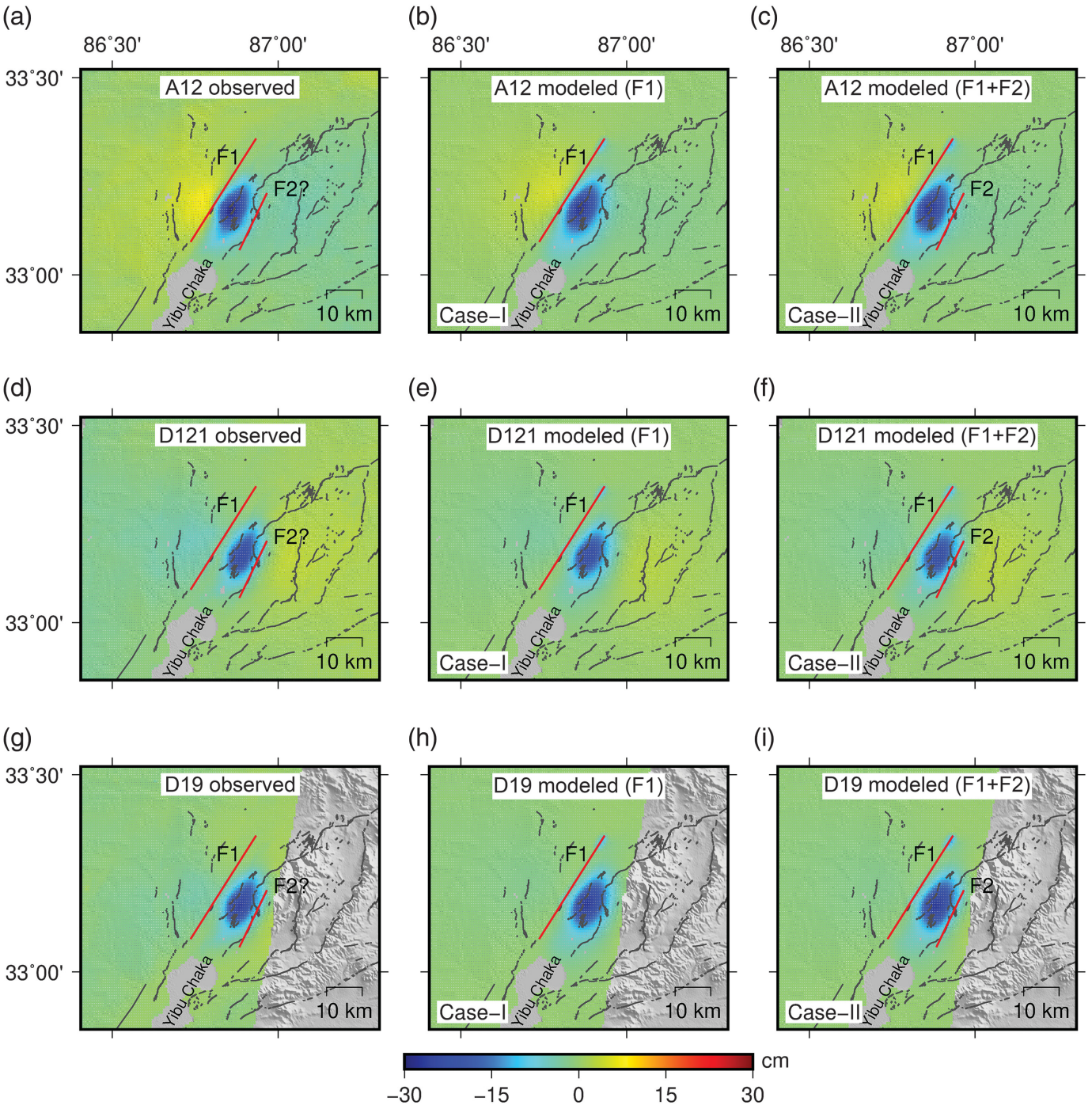

Figure 4. Predicted coseismic displacement for the case-I and case-II models. (a–c) Displacement of (a) observed, (b) modeled by the single F1, and (c) modeled by F1 + F2 for the ascending orbit of A12. Panels (d–f) similar to panels (a–c), but for the descending orbit D121. Panels (g–i) similar to panels (a–c), but for the descending orbit D19. The corresponding residual refers to Figure S9.

a single-fault model based on ⍰6 mo measurement after the mainshock (Yang et al. 2021).

The uncertainties for the inverted KA and coseismic slip were both estimated by the Monte Carlo simulation of correlated noise method (Parsons et al., 2006; Hong et al., 2022). The estimated uncertainties (Fig. S11) for the inverted KA and coseismic slip are smaller than 10% of the fault slip amplitudes (Figs. 3, 5b).

Stress-driven afterslip

Afterslip can also be predicted by the change of Coulomb failure stress by coseismic rupture based on rate-and-state friction (e.g., Ruina, 1983; Marone et al., 1991; Marone, 1998), sometimes called the "stress-driven afterslip" (abbreviated as SA in this study; e.g., Freed et al., 2006; Zhao et al., 2022). We used the code Relax version 1.0.7 (v.1.0.7; Barbot

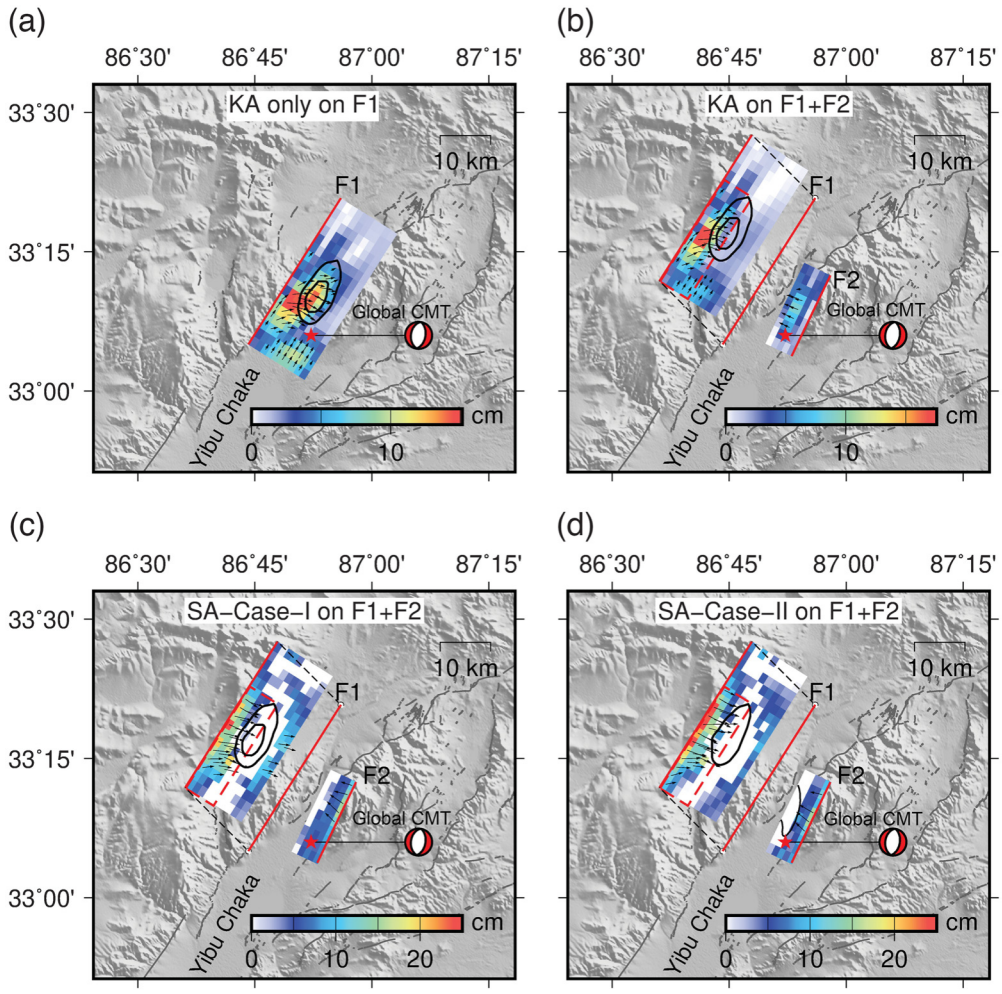

Figure 5. (a–b) Kinematic afterslip (KA) models inverted, based on (a) the single-fault of F1 and (b) the double-fault of F1 + F2. (c–d) Stress-driven afterslip (SA) models on the F1 and F2, predicted by (c) the single-fault coseismic rupture (this scenario is named SA-case-I) and (d) the double-fault coseismic rupture (named SA-case-II). Black arrows represent the rake angle and magnitude of afterslip. Black contour lines indicate the coseismic slip. Dashed red rectangle in panels (b–d) indicates the main area of afterslip, which is used to estimate moment release by afterslip; the area is shallower than the coseismic-slip zone (black contours).

and Fialko, 2010a, b) to calculate SA on F1 and F2, based on two scenarios of coseismic slip: the single-fault rupture (case-I, Fig. 3a) and the double-fault rupture (case-II, Fig. 3b). The corresponding SA for these two scenarios is referred to as SA-case-I and SA-case-II in this study. The SA should follow a rate-strength constitutive law with V $2V_0 \times \sinh\Delta\tau=fa - bg\sigma$ (Barbot and Fialko, 2010a). Significant displacement time series on 56 points (Fig. S12) in the deformation center of the A12, D121, and D19 tracks were selected to resolve the parameters of reference slip rate (V_0) and reference stress ([a–b]σ), by a grid-search method assuming a dimensionless ratio NN $\Delta\tau=a-b\sigma$ from 1 to 7. Value of V_0 was searched from 0.01 to 0.3 m/yr for F1 and 0.01 to 0.6 m/yr for F2. The crustal model was assumed to be a uniform elastic half-space for afterslip simulation in Relax. F1 and F2 were also discretized into patches with a size of ? 2 km × 2 km. More details of the SA simulation are provided in Text S4.

For SA-case-I, the relatively optimal parameters are 0.1 m/yr for V_0 and 0.52 MPa for $a-b\times\sigma$ for F1, and 0.30 m/yr for V_0 and 0.54 MPa for $a-b\times\sigma$ for F2 (Fig. S13a,b). The residuals of displacement from the double-fault model are lower than those of the single-fault model (Fig. 7). The predominant SA on F1 is at the top-left corner of the fault plane (Fig. 5c), which is similar to the KA model (Fig. 5b), despite some minor SA occurring in a deeper area than the coseismic rupture. The SA and KA on F1 and F2 are generally consistent in terms of their position and magnitude. In this case, F2 has no coseismic rupture, and its afterslip is triggered by stress change from coseismic rupture of F1.

For SA-case-II, the relatively optimal parameters are 0.15 m/yr for V_0 and 0.46 MPa for $a-b\times\sigma$ for F1, and 0.20 m/yr for V_0 and 0.38 MPa for $a-b\times\sigma$ for F2 (Fig. S13c,d). The residuals of displacement time series for SA-case-II also favor the double-fault model (Fig. S14). The SA in this case (Fig. 5d) is also generally consistent with the KA model (Fig. 5b) and SA-case-I model (Fig. 5c). In this case, F1 and F2 ruptured simultaneously, and the afterslip on F1 and F2 is triggered mainly by the coseismic rupture on the respective fault.

The predicted accumulated postseismic displacement of the A12, D121, and D19 tracks by the SA-case-I and SA-case-II models is illustrated in Figures 8 and 9, respectively. The SA on the double-fault (F1 + F2) explains the postseismic displacements better than that on the single-fault (F1), especially for that of D121 and D19 tracks, as evidenced by the residual distribution (Figs. S15, S16). In addition, there are slightly higher residuals on the D121 and D19 track for SA-case-II (Fig. S16d,f) than that for SA-case-I (Fig. S15d,f).

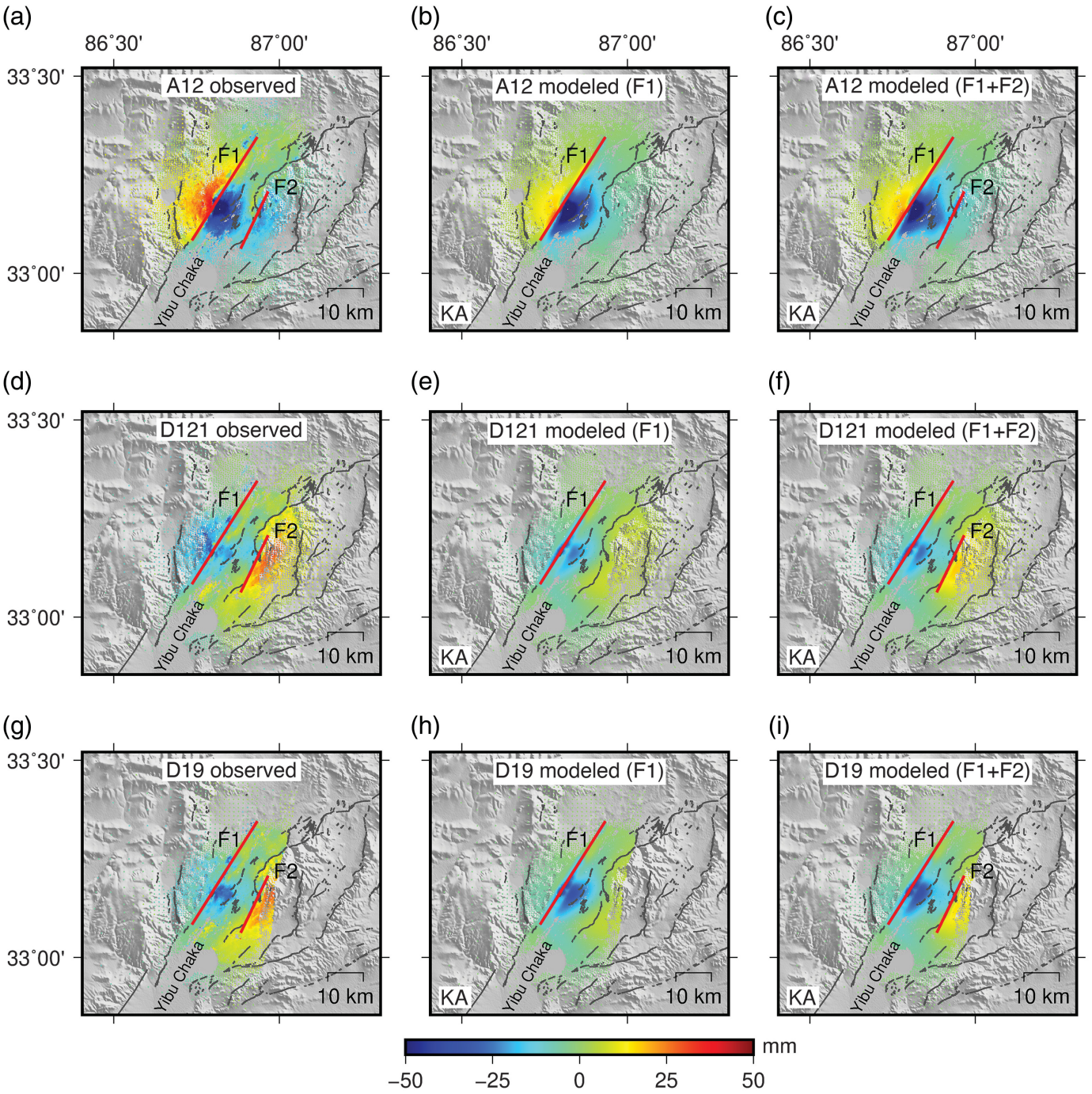

Figure 6. Predicted postseismic displacements and their residuals by the inverted KA on the single fault (F1) or the double faults (F1 + F2). (a–c) Displacements of (a) observed, (b) modeled by afterslip on F1, and (c) afterslip on F1 + F2 for the ascending orbit of A12. Panels (d–f) similar to panels (a–c), but for the descending orbit of D121. Panels (g–i) similar to panels (a–e), but for the descending orbit of D19. The corresponding residuals are shown in Figure S10.

In contrast, the residuals of A12 track for the SA-case-II (Fig. S16b) are clearly smaller than that for the SA-case-I (Fig. S15b). Although these results seem to favor coseismic rupture on both F1 and F2, we cannot reject either model. On the other hand, our results indicate that afterslip on F2 can be triggered by coseismic rupture on F1 alone or by rupture on F1 and F2 simultaneously.

Evolution of moment release on F1 and F2

We further resolved the time series of SA and estimated the evolution of seismic moment release on F1 and F2. The seismic moment released on F1 was summed over the main postseismic slip area (dashed rectangle in Fig. 5c,d), similar to that in the models of KA. An equation of F c × log1 T=τ was

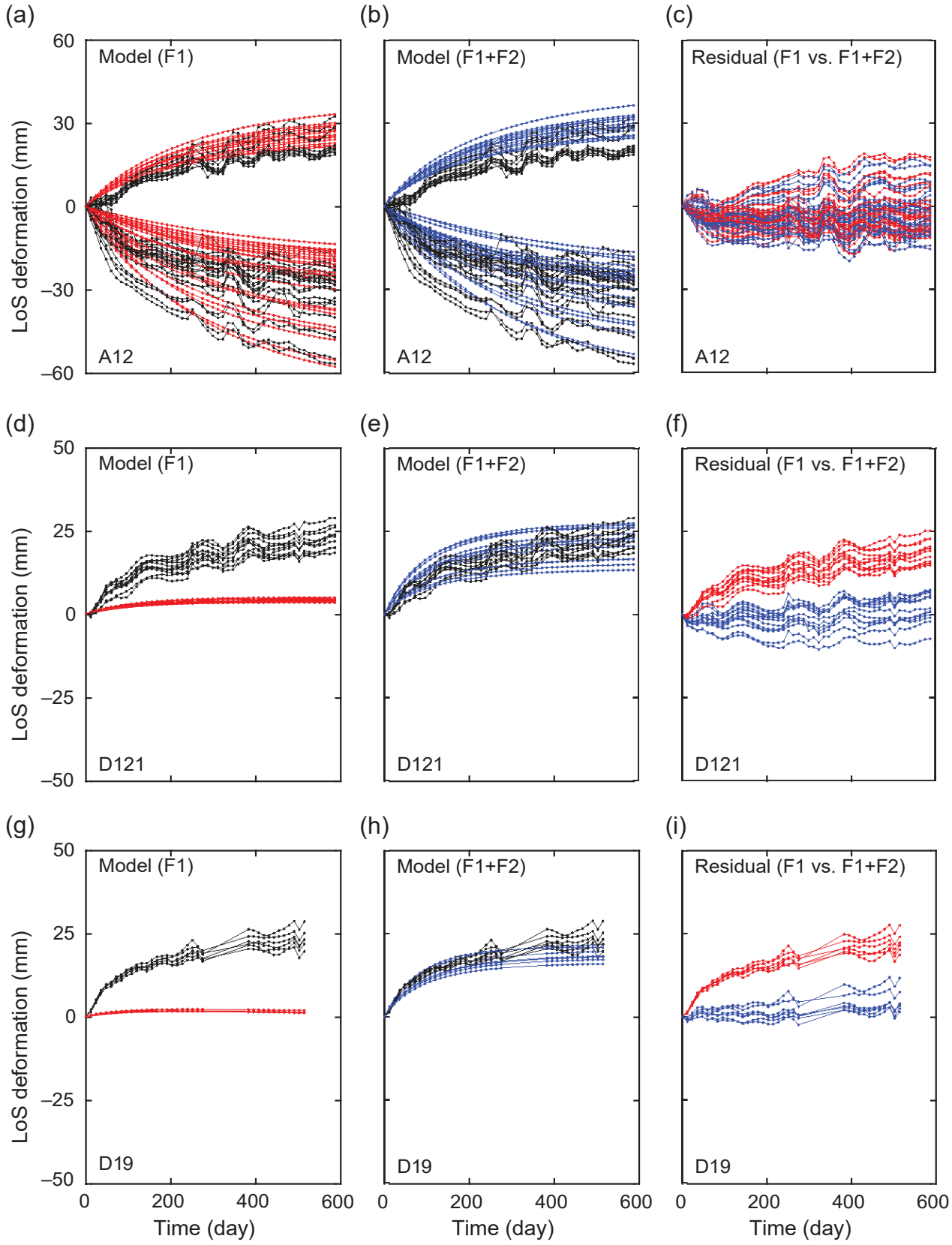

Figure 7. Comparison of the postseismic displacement time series between the observations and model predictions at the selected points (SA-case-I). (a–c) The modeled displacement sequences assuming afterslip on (a) F1 or on (b) F1 + F2, and (c) their corresponding residuals, for the selected points in the A12 track. Panels (d–f) similar to panels (a–c), but for the selected points in the D121 track. Panels (g–i) similar to panels (a–c), but for those points in the D19 track. Black lines represent the observed displacement sequences; red lines represent modeled displacement sequences assuming afterslip only on F1; blue lines represent modeled displacement sequences assuming afterslip on both the F1 and F2. The locations of the selected points are shown in Figure S12.

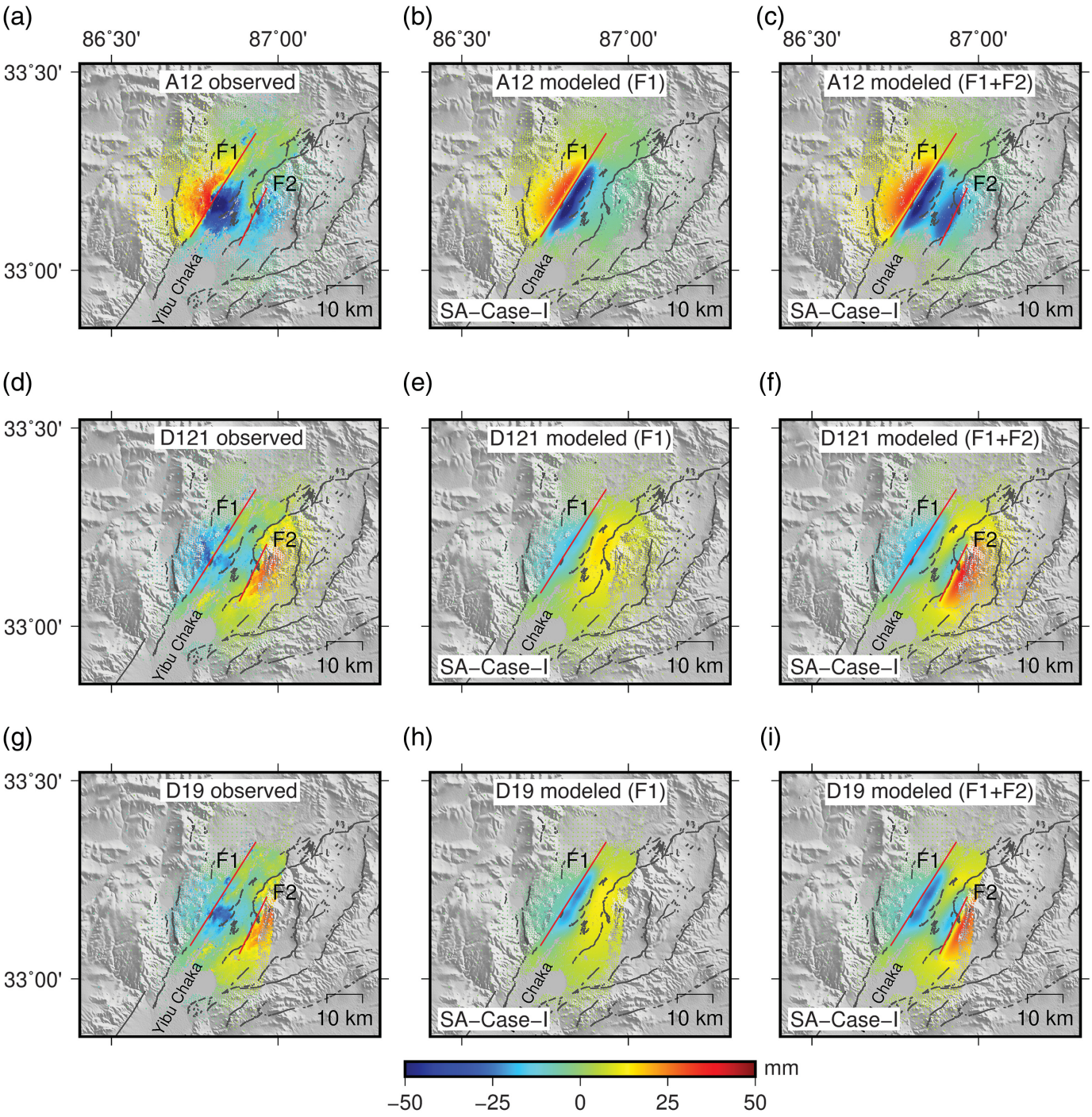

selected to fit the released seismic moment, in which c is a constant, T is the observation time, and τ is the decay coefficient (in unit of days). Our results (Fig. 10) show that the decay time (τ) of seismic moment release on F2 is shorter than that of F1. The cumulative moment released by SA was about $5{:}58 \times 10^{17}$ N · m for F1 and $2{:}98 \times 10^{17}$ N · m for F2 in SA-case-I model, or about $6{:}03 \times 10^{17}$ N · m for F1 and $2{:}42 \times 10^{17}$ N · m for F2 in SA-case-II model. The total moment released on F1 and F2 is approximately 19% of that by the coseismic slip, slightly larger than that estimated by the kinematically inverted afterslip.

Figure 8. Predicted postseismic displacements and their residuals by the SA-case-I model, which assumes that afterslip on F1 and F2 is triggered by rupture of F1 alone (Fig. 3a). (a–c) Displacements of (a) observed, (b) modeled by afterslip on F1, and (c) on F1 and F2 for the A12 track; panels (d–f) similar to panels (a–c), but for the D121 track; panels (g–i) similar to panels (a–e), but for the D19 track. The corresponding residuals are referred to Figure S15.

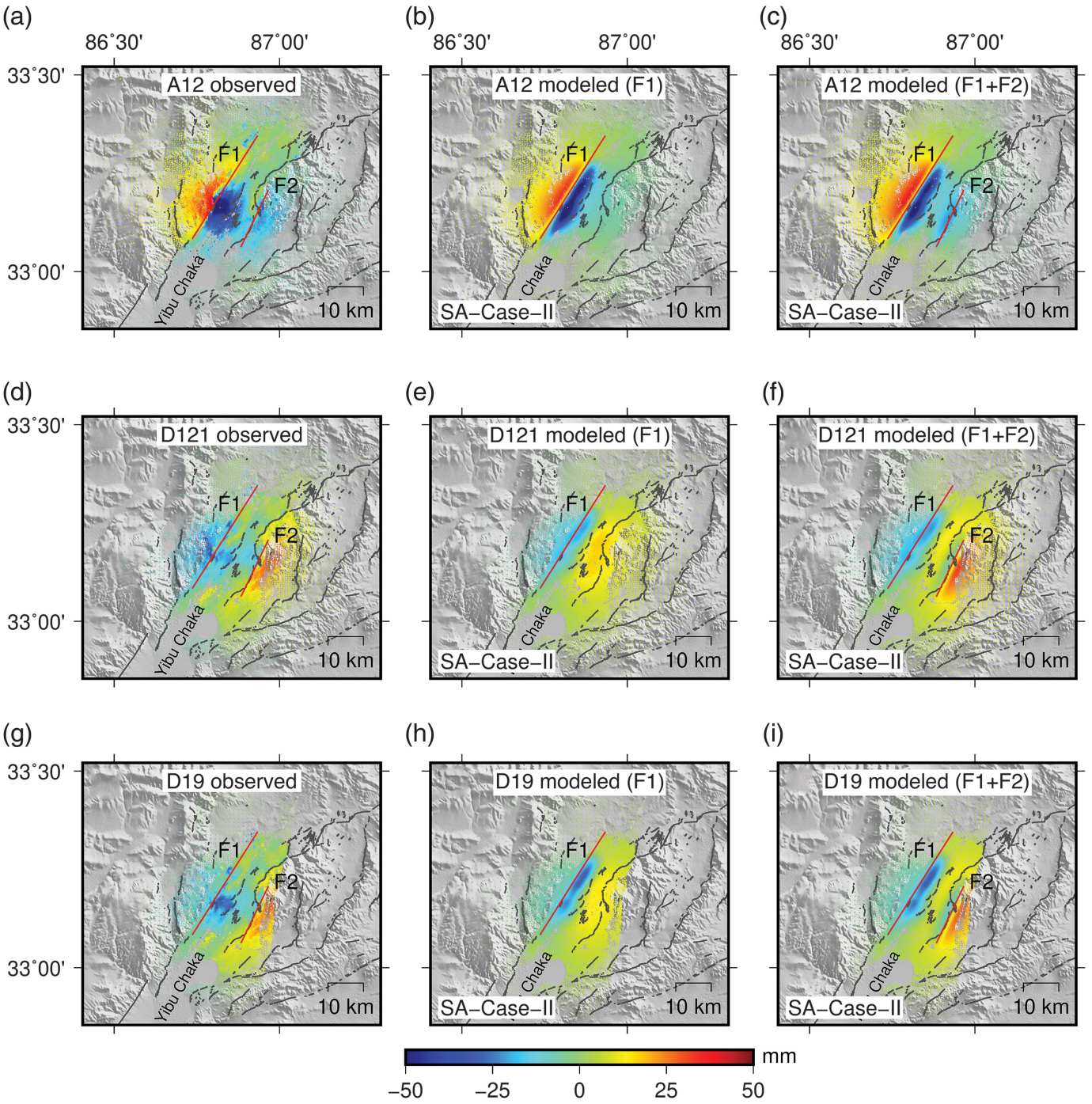

Figure 9. Similar to Figure 8, but for the SA-case-II model, which assumes that afterslip on F1 and F2 was driven by coseismic rupture of each fault (Fig. 3b). The corresponding residuals are shown in Figure S16.

DISCUSSION

The cause of the second postseismic deformation center

A key result of this study is the second postseismic deformation center in the epicentral region, ~12 km east to the seismic fault of the 2022 Nima earthquake. Gao et al. (2022) noticed this feature with a four-month observation of the D121 track but could not explain it with their afterslip model of a single curved fault. They speculated poroelastic rebound and/or viscoelastic relaxation as the possible causes. However, the effect of poroelastic rebound (up to ~3 mm of subsidence) and/or viscoelastic relaxation (up to ~10 mm of uplift) for this event is limited (Yang et al., 2021).

To test whether or not the displacement signals in the second deformation center existed before the 2022 Nima earthquake, we used the preseismic Sentinel-1A/B data from 2016 to 2020 to extract an annual displacement rate in the same three-viewing

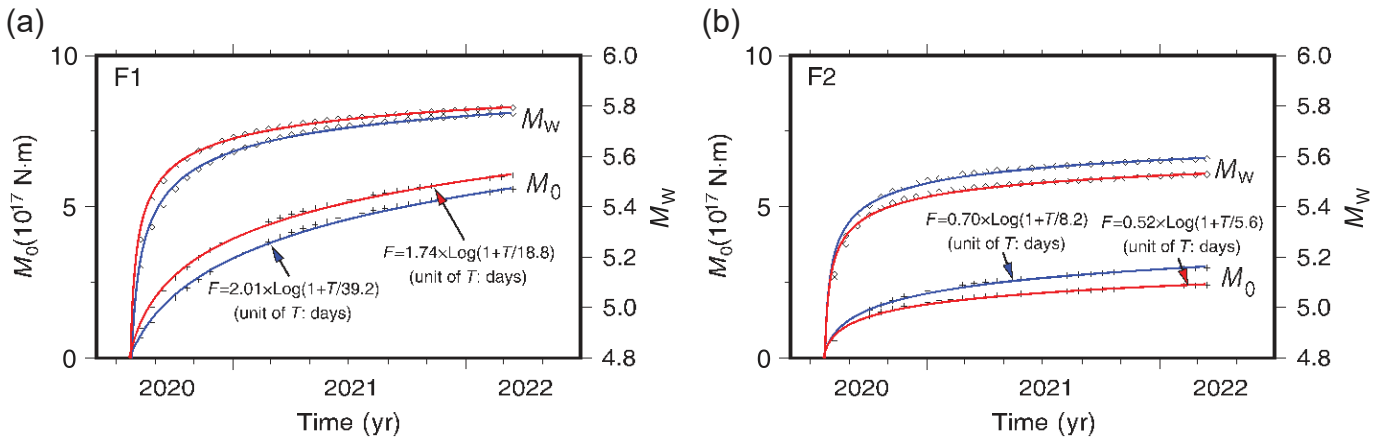

Figure 10. Evolution of seismic moment release and equivalent magnitude (taking the shear modulus to be 30 GPa) on (a) F1 and (b) F2, estimated by the SA model. For the SA-case-I model, the decay time of the moment release was about 39 days for F1 and 8 days for F2 (blue lines). For the SA-case-II model, the decay time was about 19 days for F1 and 6 days for F2 (red lines).

geometry (Fig. S17). Altogether, 87 acquisitions for the A12 track, 79 acquisitions for the D121 track, and 88 acquisitions for the D19 track were used to solve the displacement rate, by the similar processing method of PS-InSAR (Hooper et al., 2007, 2012). The displacement rate resolved by ~4 yr pre-seismic data verifies that there were no notable displacement signals near F2 and F1 before the earthquake (Fig. S17).

Gao et al. (2022) used a curved fault model with a fixed dip (49°) to fit coseismic slip and afterslip on F1, although their model cannot account for the second deformation center. We explored an F1 with variable dip and different width to see if it could explain the second postseismic displacement center. We constructed an F1 fault plane with four listric-fault geometry in a width of 20 or 40 km to invert the KA. The top- and bottom-dip angles for the four listric-fault F1 are 70° and 30°, 60° and 40°, 40° and 60°, 30° and 70°. The displacement residuals from these fault structures for the D121 track are shown in Figure S18 as an example. These results indicate that variations of the dip and width of F1 cannot explain the second postseismic deformation center (Fig. S18). Thus, we conclude that the second center of postseismic displacement in the D121 and D19 tracks (Fig. 2e,f) is caused by afterslip on a secondary fault F2 (Figs. 7–9).

Possibility of triggering afterslip on more faults

Figure 1 indicates that there are numerous faults on the eastern side of the Yibu Chaka basin. To test whether afterslip was also triggered on these faults in addition to F2, we added three additional faults east of the Yibu Chaka basin in our SA model, assuming the same initial slip rate (V_0) and reference stress $a - b \times \sigma$ as for F2. Both the SA-case-I and SA-case-II on these faults were simulated (Fig. S19). Figure S19a,b indicates negligible SA on the three additional faults. As an example, Figure S19c,d shows that the predicted postseismic displacements of D121 by the SA on multiple faults are close to those of the double faults (Figs. 8f, 9f). Although we cannot rule out the possibility of triggered afterslip on additional faults, they are not required for the interpretation of the second postseismic displacement center.

Postseismic displacement as an indicator of seismic fault structure

Usually, the seismic fault can be resolved by coseismic InSAR deformation fields, which can then be used to model the successive postseismic-slip behavior. For the 2020 M_w 6.3 Nima earthquake, our results, as well as other studies, show a single fault is sufficient to explain the coseismic deformation measured by InSAR (Li, Li, Tapponnier, et al., 2021; Li, Li, Tan, and Lu, 2021; Ji et al., 2021; Qiu et al., 2021). However, the postseismic displacements cannot be explained by the afterslip on the single-fault model. Our results show that a y-shaped double-fault structure should be responsible for the postseismic deformation, as indicated by the secondary postseismic displacement center and afterslip by kinematic inversion (Fig. 6) or stress-driven forward modeling (Figs. 7–9). This indicates that postseismic deformation is useful to reveal seismic fault structure, especially for events that happened within a complex tectonic environment.

Earthquake-triggered rupture on other faults is common, such as the 1997 Pakistan earthquake (Nissen et al., 2016), the 1999 İzmit earthquake (Wright et al., 2001), and the 2016 MeiNong earthquake (Huang et al., 2016). Such triggered rupture may be related to static or dynamic Coulomb stress change (e.g., Freed, 2005), or a high-pressure and high-stress background (Huang et al., 2016). However, measurement of coseismic deformation alone is difficult to detect the triggered ruptures on minor faults, especially if the rupture does not reach to the surface and/or if its displacement signal is obscured by that of the main rupture. Postseismic deformation may provide useful constraints for detecting triggered rupture. For the 2022 Nima earthquake, we cannot resolve whether or not coseismic

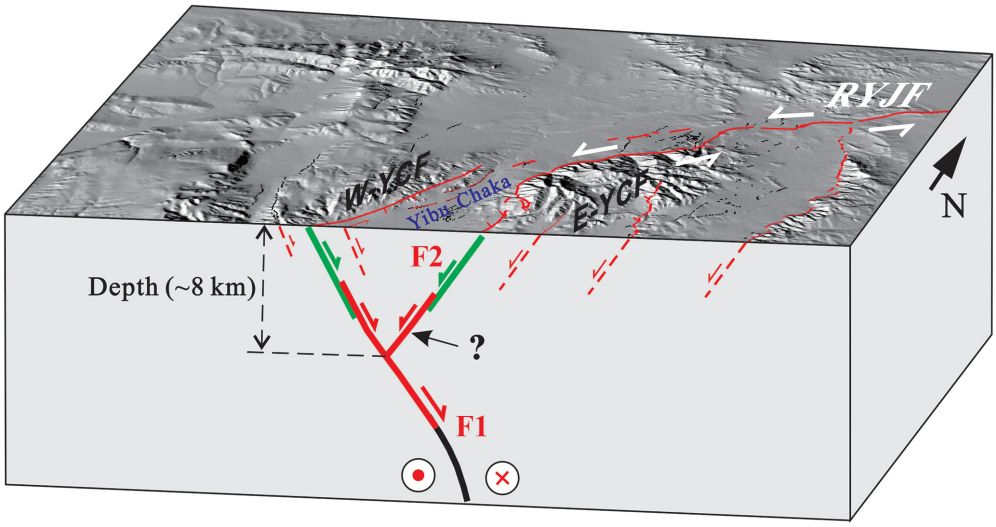

Figure 11. Schematic diagram of the coseismic rupture and successive afterslip on the y-shape double fault in a negative flower structure. Red and green lines on F1 and F2 represent the coseismic slip and afterslip area, respectively. Coseismic rupture of F2 is not required by the data. Afterslip occurred on shallower areas than the coseismic slip.

rupture was triggered on F2 (Fig. 3b) from the coseismic deformation field (Fig. 4), but it is likely from the postseismic deformation and SA test (Fig. 9c vs. Fig. 8c). The afterslip on F2, either induced by coseismic rupture of F1 or rupture on F2 itself, provides a new explanation for the seismic fault structure that is more complex than in previous studies (e.g., Li, Li, Tapponnier, et al., 2021; Gao et al., 2022).

Complex rupture and afterslip in the extending central Tibetan plateau

The postseismic deformation fields resolved in this study revealed a secondary displacement center that is indicative of afterslip on a second fault F2, probably an antithetic fault that connects with the main fault F1 at depth to form a y-shaped pair of conjugate faults in a negative flower structure (Fig. 11). Afterslip on F2 may be caused by coseismic rupture of both F1 and F2, which would make the 2020 Nima earthquake an example of simultaneous or possibly triggered rupture of a conjugate pair of normal faults. Recent studies have found many earthquakes that ruptured multiple fault segments, such as the 2016 Kaikōura earthquake in New Zealand (Hamling et al., 2017), or conjugate faults, such as the 2019 Ridgecrest earthquake in California (Ross et al., 2019). These complex ruptures call for rethinking of earthquake hazard assessment, which usually considers rupture of a single fault. Most of the reported complex ruptures occurred on strike-slip faults; complex rupture of a normal fault system has been rarely reported. Alternatively, afterslip on F2 may be triggered by coseismic slip only on F1, which would make an interesting case of afterslip caused by rupture of another fault. Afterslip triggered by rupture of another fault is rare but possible, such as the 1989 Loma Prieta earthquake (Segall et al., 2000).

In either case, the coseismic rupture and afterslip of the 2020 Nima earthquake revealed by our results, in addition to previous studies (e.g., Li, Li, Tapponnier, et al., 2021; Yang et al., 2021; Gao et al., 2022), provide useful insights into active extension in the central Tibetan plateau. Although the Indo–Eurasian plate convergence continues, crustal deformation within the Tibetan plateau has been dominated by east–west extension since middle Miocene, driven by gravitational collapse (Liu and Yang, 2003) and kinematically related to lateral crustal extrusion along strike-slip faults (Yin, 2000). The 2020 Nima earthquake and afterslip demonstrated an event where extension occurred on a pair of normal faults bounding a small pull-apart basin formed in a releasing stepover of the sinistral RYJF.

CONCLUSIONS

We used the Sentinel-1 data to resolve the coseismic and ⍰19 months of postseismic deformation of the 2022 Nima earthquake. The results show a secondary postseismic displacement center ⍰12 km to the east of the main seismogenic fault and can be best explained by afterslip on a secondary fault, probably an antithetic fault that connected with the main fault at depth in a negative flower structure in the Yibu Chaka pull-apart basin. Afterslip on the secondary fault could be caused by coseismic rupture on the same fault, making the 2020 Nima earthquake an example of simultaneous rupture of conjugate faults in a system of normal faults. Alternatively, afterslip in the secondary fault could be triggered by coseismic rupture on the main fault, illustrating complex causes of afterslip. Because coseismic rupture on the secondary fault cannot be resolved from the available coseismic InSAR data, afterslip on a conjugate fault is clearly preferred for fitting the postseismic deformation. These results illustrate complex fault slip of the Nima earthquake and active crustal extension in the central Tibetan plateau.

DATA AND RESOURCES

The Interferometric Synthetic Aperture Radar (InSAR) postseismic displacement sequences, coseismic displacements, and the related slip model used in this study are publicly available at figshare.com/s/

a77d972a28b5ad9e17ea. The Sentinel-1 single look complex (SLC) data were provided by the European Space Agency (ESA), and downloaded from the Alaska Satellite Facility (https://search.asf.alaska.edu/#/). The focal mechanism solutions of historical earthquake, mainshock, and aftershock come from the Global Centroid Moment Tensor project (Global CMT; https://www.globalcmt.org/CMTsearch.html). The three months aftershocks data are from the China Earthquake Data Center (CEDC; https://data.earthquake.cn/datashare/login.jsp; available only in Chinese and user registration is required). All websites were last accessed in March 2023. The supplemental material for this article includes four text files, 19 figures, and three tables.

DECLARATION OF COMPETING INTERESTS

The authors acknowledge that there are no conflicts of interest recorded.

ACKNOWLEDGMENTS

The authors thank two anonymous reviewers and associate editor Richard Briggs for their constructive comments and suggestions. This study is supported by the National Key R&D Program of China (Grant Number 2019YFE0108900), the National Natural Science Foundation of China (Grant Numbers 41874013, 42074091, and 41874024), and the high-resolution remote sensing program (Grant Number 31-Y30F09-9001-20/22). Liu acknowledges support from the National Science Foundation (NSF; Grant Number 2013656). The authors thank Anhui Sun and Tai Liu from the Institute of Earthquake Forecasting, China Earthquake Administration (CEA) for the discussion of fault model. Most of the figures were generated with the Generic Mapping Tools (GMT).

REFERENCES

Avouac, J.-P. (2015). From geodetic imaging of seismic and aseismic fault slip to dynamic modeling of the seismic cycle, Annu. Rev. Earth Planet. Sci. **43**, 233–271.

Barbot, S., and Y. Fialko (2010a). A unified continuum representation of post-seismic relaxation mechanisms: Semi-analytic models of afterslip, poroelastic rebound and viscoelastic flow, Geophys. J. Int. **182**, 1124–1140.

Barbot, S., and Y. Fialko (2010b). Fourier-domain Green's function for an elastic semi-infinite solid under gravity, with applications to earthquake and volcano deformation, Geophys. J. Int. **182**, 568–582.

Barnhart, W. D., C. M. J. Brengman, S. Li, and K. E. Peterson (2018). Ramp-flat basement structures of the Zagros mountains inferred from co-seismic slip and afterslip of the 2017 Mw7.3 Darbandikhan, Iran/Iraq earthquake, Earth Planet. Sci. Lett. **496**, 96–107.

Bassin, C., G. Laske, and G. Masters (2000). The current limits of resolution for surface wave tomography in North America, Eos Trans. AGU **81**, F897.

Chen, C. W., and H. A. Zebker (2002). Phase unwrapping for large SAR interferograms: Statistical segmentation and generalized network models, IEEE Trans. Geosci. Remote Sens. **40**, 1709–1719.

Ferretti, A., C. Prati, and F. Rocca (2001). Permanent scatterers in SAR interferometry, IEEE Trans. Geosci. Remote Sens. **39**, 8–20.

Freed, A. M. (2005). Earthquake triggering by static, dynamic, and postseismic stress transfer, Annu. Rev. Earth Planet. Sci. **33**, 335–367.

Freed, A. M., R. Bürgmann, E. Calais, J. Freymueller, and S. Hreinsdóttir (2006). Implications of deformation following the 2002 Denali, Alaska, earthquake for postseismic relaxation processes and lithospheric rheology, J. Geophys. Res. **111**, doi: 10.1029/2005JB003894.

Gao, H., M. Liao, X. Liang, G. Feng, and G. Wang (2022). Coseismic and postseismic fault kinematics of the July 22, 2020, Nima (Tibet) Ms6.6 earthquake: Implications of the forming mechanism of the active N-S-trending grabens in Qiangtang, Tibet, Tectonics **41**, doi: 10.1029/2021TC006949.

Hamling, I. J., S. Hreinsdóttir, K. Clark, J. Elliott, C. Liang, E. Fielding, N. Litchfield, P. Villamor, L. Wallace, T. J. Wright, et al. (2017). Complex multifault rupture during the 2016 Mw 7.8 Kaikōura earthquake, New Zealand, Science **356**, eaam7194, doi: 10.1126/science.aam7194.

Harding, T. P. (1985). Seismic characteristics and identification of negative flower structures, positive flower structures, and positive structural inversion, AAPG Bull. **69**, 582–600.

Hong, S., and M. Liu (2021). Postseismic deformation and afterslip evolution of the 2015 Gorkha earthquake constrained by InSAR and GPS observations, J. Geophys. Res. **126**, e2020JB020230, doi: 10.1029/2020JB020230.

Hong, S., M. Liu, T. Liu, Y. Dong, L. Chen, G. Meng, and Y. Xu (2022). Fault source model and stress changes of the 2021 M_w 7.4 Maduo earthquake, China, constrained by InSAR and GPS measurements, Bull. Seismol. Soc. Am. **112**, 1284–1296.

Hooper, A., and H. A. Zebker (2007). Phase unwrapping in three dimensions with application to InSAR time series, J. Opt. Soc. Am. **24**, 2737–2747.

Hooper, A., D. Bekaert, K. Spaans, and M. Arıkan (2012). Recent advances in SAR interferometry time series analysis for measuring crustal deformation, Tectonophysics **514/517**, 1–13.

Hooper, A., P. Segall, and H. Zebker (2007). Persistent scatterer interferometric synthetic aperture radar for crustal deformation analysis, with application to Volcán Alcedo, Galápagos, J. Geophys. Res. **112**, doi: 10.1029/2006JB004763.

Huang, M.-H., H. Tung, E. J. Fielding, H.-H. Huang, C. Liang, C. Huang, and J.-C. Hu (2016). Multiple fault slip triggered above the 2016 Mw6.4 MeiNong earthquake in Taiwan, Geophys. Res. Lett. **43**, 7459–7467.

Ji, Z.-T., Y.-Z. Zhang, and S.-J. Wang (2021). Coseismic deformation field and fault slip distribution inversion of the Ms 6.6 Nima, Xizang earthquake by Sentinel-1A InSAR data, Prog. Geophys. **36**, 2312–2319 (in Chinese).

Li, C. T., Q. Li, K. Tan, and X. Lu (2021). Coseismic deformation characteristics of the 2020 Nima, Xizang Mw 6.3 earthquake from Sentinel-1A/B InSAR data and rupture slip distribution, Chin. J. Geophys. **64**, 2297–2310 (in Chinese).

Li, K., Y. Li, P. Tapponnier, X. Xu, D. Li, and Z. He (2021). Joint InSAR and field constraints on faulting during the M_w 6.4, July 23, 2020, Nima/Rongma earthquake in central Tibet, J. Geophys. Res. **126**, doi: 10.1029/2021JB022212.

Liu, M., and Y. Yang (2003). Extensional collapse of the Tibetan Plateau: Results of three-dimensional finite element modeling, J. Geophys. Res. **108**, doi: 10.1029/2002JB002248.

Marone, C. (1998). The effect of loading rate on static friction and the rate of fault healing during the earthquake cycle, Nature 391, 69–72.

Marone, C., C. Scholz, and R. Bilham (1991). On the mechanics of earthquake afterslip, J. Geophys. Res. 96, 8441–8452.

Massonnet, D., M. Rossi, C. Carmona, F. Adragna, G. Peltzer, K. Feigl, and T. Rabaute (1993). The displacement field of the Landers earthquake mapped by radar interferometry, Nature 364, 138–142.

Maurer, J., R. Dutta, A. Vernon, and S. Vajedian (2022). Complex rupture and triggered aseismic creep during the 14 August 2021 Haiti earthquake from satellite geodesy, Geophys. Res. Lett. 49, doi: 10.1029/2022GL098573.

Nissen, E., J. R. Elliott, R. A. Sloan, T. J. Craig, G. J. Funning, A. Hutko, B. E. Parsons, and T. J. Wright (2016). Limitations of rupture forecasting exposed by instantaneously triggered earthquake doublet, Nature Geosci. 9, 330–336.

Parsons, B., T. Wright, P. Rowe, J. Andrews, J. Jackson, R. Walker, M. Khatib, M. Talebian, E. Bergman, and E. R. Engdahl (2006). The 1994 Sefidabeh (eastern Iran) earthquakes revisited: New evidence from satellite radar interferometry and carbonate dating about the growth of an active fold above a blind thrust fault, Geophys. J. Int. 164, 202–217.

Qiu, J-T., L-Y. Ji, L. Liu, and C-J. Liu (2021). InSAR coseismic deformation and tectonic implications for the 2020 Mw 6.3 Nima earthquake in Xizang, Seismol. Egol. 43, 1586–1599 (in Chinese).

Rosen, P. A., E. Gurrola, G. F. Sacco, and H. Zebker (2012). The InSAR scientific computing environment, EUSAR 2012 9th European Conference on Synthetic Aperture Radar, 730–733.

Ross, Z. E., B. Idini, Z. Jia, O. L. Stephenson, M. Zhong, X. Wang, Z. Zhan, M. Simons, E. J. Fielding, S.-H. Yun, et al. (2019). Hierarchical interlocked orthogonal faulting in the 2019 Ridgecrest earthquake sequence, Science 366, 346–351.

Ruina, A. (1983). Slip instability and state variable friction laws, J. Geophys. Res. 88, 10,359–10,370.

Segall, P., R. Bürgmann, and M. Matthews (2000). Time-dependent triggered afterslip following the 1989 Loma Prieta earthquake, J. Geophys. Res. 105, 5615–5634.

Simons, M., Y. Fialko, and L. Rivera (2002). Coseismic deformation from the 1999 Mw 7.1 Hector Mine, California, earthquake as inferred from InSAR and GPS observations, Bull. Seismol. Soc. Am. 92, 1390–1402.

Taylor, M., A. Yin, F. J. Ryerson, P. Kapp, and L. Ding (2003). Conjugate strike-slip faulting along the Bangong-Nujiang suture zone accommodates coeval east-west extension and north-south shortening in the interior of the Tibetan Plateau, Tectonics 22, doi: 10.1029/2002TC001383.

Van der Elst, N. J., and E. E. Brodsky (2010). Connecting near-field and far-field earthquake triggering to dynamic strain, J. Geophys. Res. 115, doi: 10.1029/2009JB006681.

Vasyura-Bathke, H., J. Dettmer, A. Steinberg, S. Heimann, M. P. Isken, O. Zielke, P. M. Mai, H. Sudhaus, and S. Jónsson (2020). The Bayesian earthquake analysis tool, Seismol. Res. Lett. 91, 1003–1018.

Wang, K., and R. Bürgmann (2020). Probing fault frictional properties during afterslip updip and downdip of the 2017 M_w 7.3 Sarpol-e Zahab earthquake with space geodesy, J. Geophys. Res. 125, doi: 10.1029/2020JB020319.

Wang, R., F. Diao, and A. Hoechner (2013). SDM—A geodetic inversion code incorporating with layered crust structure and curved fault geometry, EGU General Assembly Conference Abstracts, Vienna, Austria, 7–12 April 2013, EGU2013-2411.

Wright, T., E. Fielding, and B. Parsons (2001). Triggered slip: Observations of the 17 August 1999 Izmit (Turkey) earthquake using radar interferometry, Geophys. Res. Lett. 28, 1079–1082.

Yang, J., C. Xu, Y. Wen, and G. Xu (2021). The July 2020 Mw 6.3 Nima earthquake, central Tibet: A shallow normal-faulting event rupturing in a stepover zone, Seismol. Res. Lett. 93, 45–55.

Yin, A. (2000). Mode of Cenozoic east-west extension in Tibet suggesting a common origin of rifts in Asia during the Indo-Asian collision, J. Geophys. Res. 105, 21,745–21,759.

Zhao, B., R. Bürgmann, D. Wang, J. Zhang, J. Yu, and Q. Li (2022). Aseismic slip and recent ruptures of persistent asperities along the Alaska-Aleutian subduction zone, Nat. Commun. 13, 3098.

Manuscript received 28 November 2022
Published online 5 May 2023